

Monoclinic microdomains and clustering in the colossal magnetoresistance manganites $\text{Pr}_{0.7}\text{Ca}_{0.25}\text{Sr}_{0.05}\text{MnO}_3$ and $\text{Pr}_{0.75}\text{Sr}_{0.25}\text{MnO}_3$

M. Hervieu, G. Van Tendeloo,* V. Caignaert, A. Maignan, and B. Raveau
*Laboratoire CRISMAT, ISMRA et Université de Caen, CNRS URA 1318, associée au CNRS,
 6 Bd du Maréchal Juin, 14050 CAEN Cedex, France*

(Received 6 November 1995; revised manuscript received 12 February 1996)

A detailed high-resolution microscopy investigation of two praseodymium manganites, $\text{Pr}_{0.7}\text{Ca}_{0.25}\text{Sr}_{0.05}\text{MnO}_3$ and $\text{Pr}_{0.75}\text{Sr}_{0.25}\text{MnO}_3$ which exhibit a resistance ratio of 2.5×10^5 at 88 K and of 7 at 210 K, respectively, is reported. Existence of monoclinic domains in the orthorhombic GdFeO_3 -type matrix and $(\text{A}^{\text{II}}\text{Mn}^{\text{IV}}\text{O}_3)_n$ clusters corresponding to a modification of the geometry of the MnO_6 octahedra has been observed; models are proposed which illustrate the high flexibility of the $[\text{MnO}_2]$ layers. [S0163-1829(96)07921-0]

INTRODUCTION

Colossal magnetoresistance (CMR) properties have been recently reported in manganese perovskites, synthesized either in the form of single crystal,¹ thin films²⁻⁹ or of ceramics.¹⁰⁻¹⁹ These compounds, which are of considerable interest for device applications, exhibit resistance ratios, $\text{RR} = R_0/R_H$ (R_0 and R_H are the resistances in zero and $\mu_0 H = 5$ T magnetic fields, respectively) up to 10^{11} .

The origin of the CMR properties is so far not really elucidated, though the influence of the size of the interpolated cations upon T_c has been demonstrated¹²⁻¹⁷ recently. One important issue deals with the relationship between the structure of these phases and their CMR properties. In other words, it has not yet been detected whether the transition from a semiconducting paramagnetic state to a metallic ferromagnetic state at decreasing temperature may be connected to a structural transition. In a recent powder neutron-diffraction study of the CMR manganites $\text{Pr}_{0.7}\text{Ca}_{0.3-x}\text{Sr}_x\text{MnO}_3$,²⁰ one observed for $x=0.05$ a transition from the paramagnetic to an antiferromagnetic and finally to a canted ferromagnetic state, accompanied by a decrease of the Jahn-Teller effect of manganese at the ferromagnetic transition. The crystallographic cell of this phase was found to be orthorhombic, isotypic with the GdFeO_3 structure. Nevertheless, due to the pseudocubic symmetry of this material, the powder neutron-diffraction data do not allow us to rule out an eventual tiny distortion of the cell. Moreover, the existence and arrangements of microdomains and defects, may play a role in the CMR properties of these materials.

We report here a detailed high-resolution microscopy investigation of two praseodymium manganites, $\text{Pr}_{0.7}\text{Ca}_{0.25}\text{Sr}_{0.05}\text{MnO}_3$ and $\text{Pr}_{0.75}\text{Sr}_{0.25}\text{MnO}_3$ which exhibit a resistance ratio (RR) of 2.5×10^5 at 88 K,¹⁴ and of 7 at 210 K,¹² respectively.

EXPERIMENT

Polycrystalline samples have been prepared by mixing Pr_6O_{11} , CaO , MnO_2 , and SrCO_3 in stoichiometric proportions according to the formula $\text{Pr}_{0.7}\text{Ca}_{0.25}\text{Sr}_{0.05}\text{MnO}_3$ and

$\text{Pr}_{0.75}\text{Sr}_{0.25}\text{MnO}_3$. The mixtures were first heated to achieve decarbonation, sintered at 1500 °C for 12 h and slowly cooled down to room temperature.

The electron-diffraction study (ED) was performed with a JEOL 200CX electron microscope fitted with a side entry goniometer ($\pm 60^\circ$); the high-resolution electron microscopy study was carried out with JEOL 2010 and TOPCON 002B microscopes operating at 200 kV; the point to point resolution of the TOPCON 002B is 1.8 Å. The microscopes are equipped with KEVEX analyzers. The EDS analyses were systematically performed on numerous grains; they showed a high homogeneity of the cation distribution within the crystals, corresponding to the nominal composition of the samples. Image calculations have been carried out with the Mac Tempas programme.

RESULTS AND DISCUSSION

Symmetry and image calculations: evidence for the existence of monoclinic microdomains in the orthorhombic matrix. The reconstruction of the reciprocal space from the ED patterns of the two samples $\text{Pr}_{0.7}\text{Ca}_{0.25}\text{Sr}_{0.05}\text{MnO}_3$ and $\text{Pr}_{0.75}\text{Sr}_{0.25}\text{MnO}_3$ (Fig. 1), has allowed an orthorhombic cell to be evidenced with the reflection conditions $0kl$, $k+l=2n$ and $hk0$, $h=2n$. The powder x-ray diffraction patterns, were then refined in an orthorhombic cell, isotypic with the GdFeO_3 structure,²¹ with the following parameters:

$$a_o = 5.4590(1) \text{ \AA}, \quad b_o = 7.6828(2) \text{ \AA},$$

$$\text{and } c_o = 5.4367(1) \text{ \AA}$$

$$\text{for } \text{Pr}_{0.7}\text{Ca}_{0.25}\text{Sr}_{0.05}\text{MnO}_3,$$

$$a_o = 5.481(1) \text{ \AA}, \quad b_o = 7.730(2) \text{ \AA},$$

$$\text{and } c_o = 5.473(1) \text{ \AA}$$

$$\text{for } \text{Pr}_{0.75}\text{Sr}_{0.25}\text{MnO}_3.$$

Most crystals exhibit ED patterns where apparently two or more variants are superposed; such effects have been observed in other perovskites involving superstructures along one of the equivalent directions of the perovskite subcell.

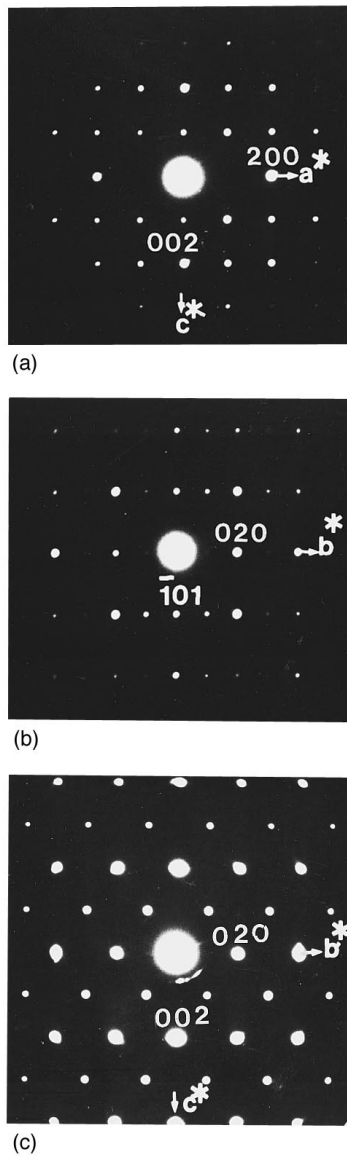


FIG. 1. Typical ED patterns of $\text{Pr}_{0.7}\text{Ca}_{0.25}\text{Sr}_{0.05}\text{MnO}_3$: (a) $[010]_o$, (b) $[101]_o$, and (c) $[100]_o$. Note that extra reflections are often observed due to double diffraction phenomena and to the existence of oriented domains.

Three examples of such ED patterns are given in Fig. 2. All patterns can be explained as a superposition of different variants of the orthorhombic structure. In Fig. 2(a), the zone axis is $[101]_o$ and the \mathbf{b}_o axes of the two domains are perpendicular; in Fig. 2(b), one observes the superposition of a $[010]_o$ and a $[101]_o$ pattern and, in Fig. 2(c), $[100]_o$ and $[001]_o$ patterns are superimposed. The problem of the size and boundary quality of these domains will be discussed in the next section but ED patterns of a single variant are usually hard to obtain.

Crystallites of the two phases have been studied by high-resolution electron microscopy (HREM) viewed along the four directions, $[010]_o$, $[001]_o$, $[100]_o$, and $[101]_o$ for which the orthorhombic structure can directly and simply be interpreted in terms of cation and oxygen columns. Images are very similar for $\text{Pr}_{0.7}\text{Ca}_{0.25}\text{Sr}_{0.05}\text{MnO}_3$ and $\text{Pr}_{0.75}\text{Sr}_{0.25}\text{MnO}_3$. The contrast interpretation has been carried out comparing the experimental images with the calcu-

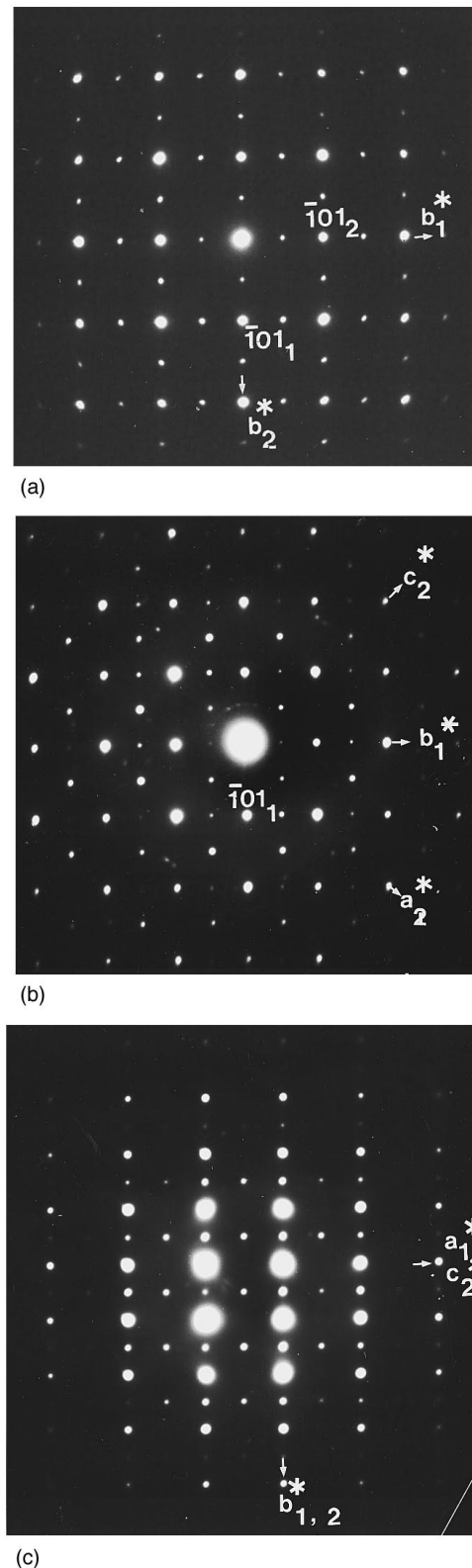


FIG. 2. Examples of ED patterns resulting from the superposition of two variants (labeled 1 and 2): (a) 90° oriented $[101]_o$ domains, (b) $[101]_o$ and $[010]_o$, and (c) $[100]_o$ and $[001]_o$.

lated ones. These images have been simulated starting from positional parameters (Table I) refined from the neutron-diffraction data.²⁰

The experimental $[101]_o$ images show a remarkable observation: besides the usual crystal thickness consideration,

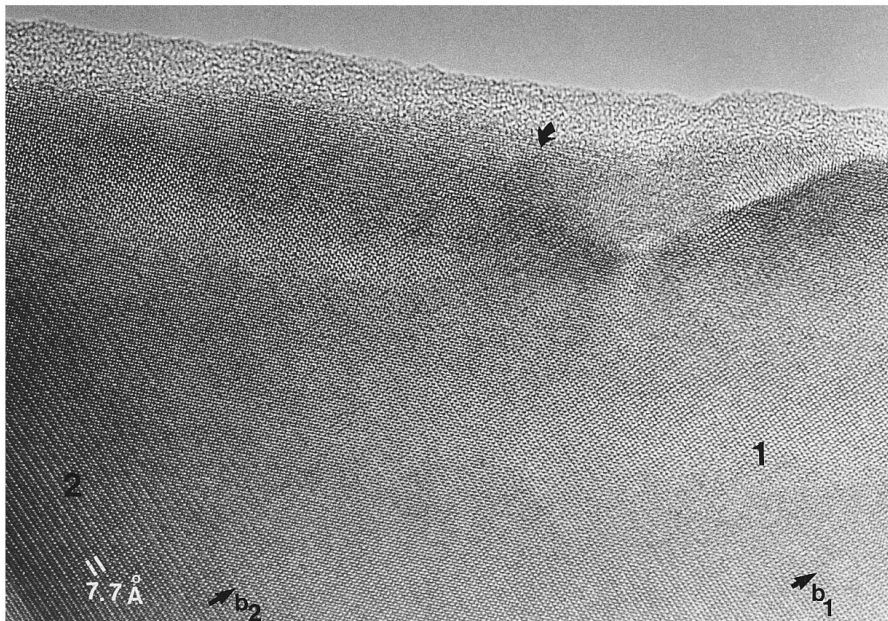
TABLE I. Atomic coordinates of $\text{Pr}_{0.7}\text{Ca}_{0.25}\text{Sr}_{0.05}\text{MnO}_3$ after neutron-diffraction data at 260 K according to Ref. 20, SG $Pnma$.

Atom	x	y	z	Occup.
Pr	0.032 91	0.25	-0.005 99	0.7
Sr	0.032 91	0.25	-0.005 99	0.05
Ca	0.032 91	0.25	-0.005 99	0.25
Mn	0.500	0.00	0.000	1.0
O(1)	0.486 45	0.25	0.070 1	1.0
O(2)	0.287 01	0.036 97	-0.286 45	1.0

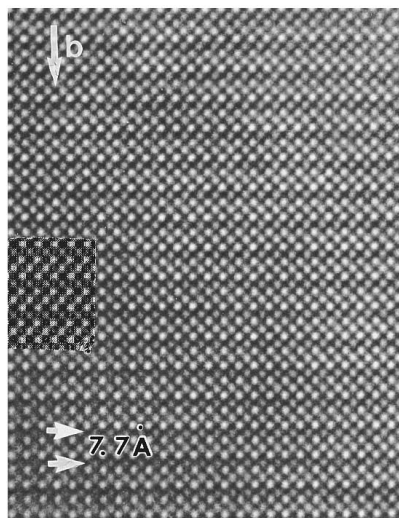
the contrast may strongly vary, depending on the crystal and even within one crystal. This is illustrated in Fig. 3(a) recorded on a thin crystal edge. In area labeled 1, a rather regular contrast is observed which mainly consists of a square array of bright spots, spaced by ≈ 2.7 Å. Such a contrast is close to that expected for a perovkite-type structure and fits with the calculated image for the orthorhombic struc-

ture in the space group (SG)- $Pnma$.²²⁻²⁴ Image calculations were carried out varying the crystal thickness from 20 to 300 Å. A part of the calculated through focus series is given in Fig. 4(a) for a crystal thickness of 12 nm and the corresponding calculated ED pattern is shown in Fig. 4(c). Such a rather high value of the thickness is presented here to make easier the discussion on the experimental contrast (other thickness values are considered in Fig. 7(a)). Clearly, the contrast variation due to the doubling of the \mathbf{b}_o axis is scarcely visible, as in area 1 of Fig. 3(a). On the contrary, the contrast in area 2 is such that it consists of a row of bright dots alternating with a row of grey dots, enhancing the periodicity of 7.7 Å. Another example of this strong 7.7 Å periodicity is given in the enlarged image displayed in Fig. 3(b). Such a variation of contrast is different from the calculated image, whatever the focus, the crystal orientation or the crystal thickness as shown for instance in Fig. 4(a).

To understand this discrepancy between the observed and the calculated images, several possibilities have been put forward. Recording the images with different TEM and study-



(a)



(b)

FIG. 3. HREM $[101]_o$ images: (a) contrast differences are observed in areas 1 and 2; in area 1, the contrast consists of a square array of 2.7 Å spaced bright dots, whereas in area 2 the 7.7 Å periodicity is enhanced. (b) enlarged image of a crystal where the 7.7 Å periodicity is established throughout the whole matrix. The theoretical image, calculated in the $P2_1/c$ space group and a focus value close to -200 Å is superimposed in the left part.

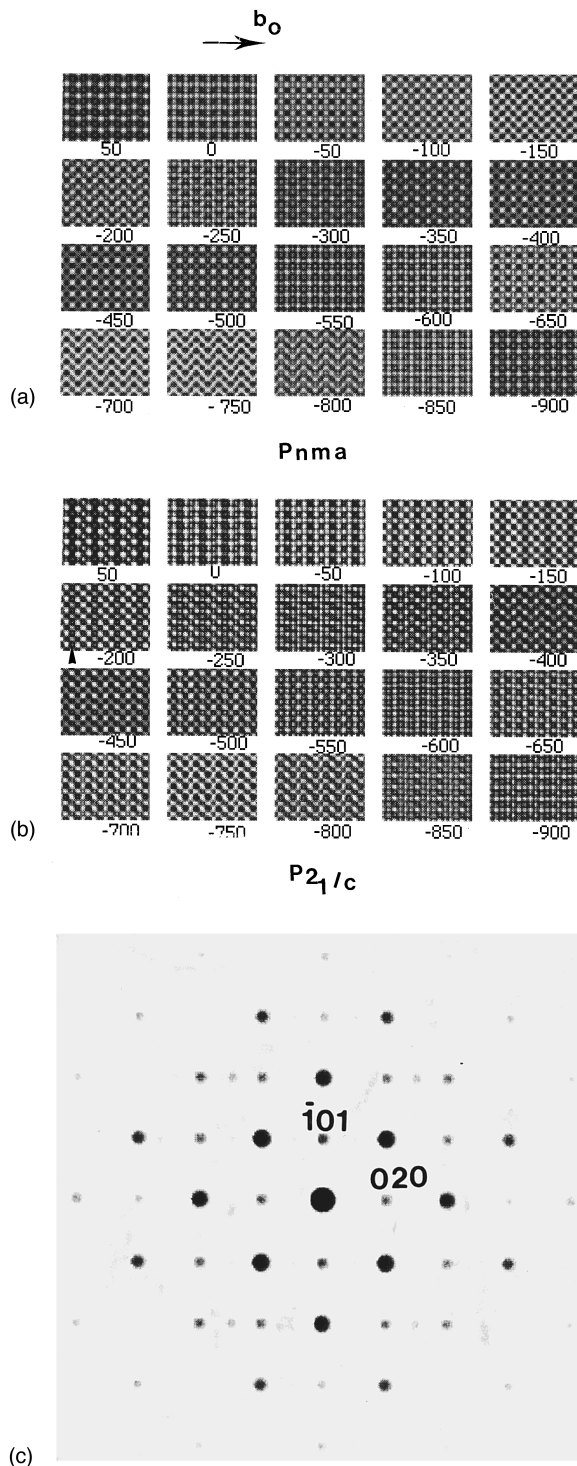


FIG. 4. (a) Orthorhombic model, space group $Pnma$: through focus series calculated for a crystal thickness close to 12 nm; the focus values are given in Å and the positional parameters are in Table I, (b) corresponding through focus series calculated for a monoclinic model, space group $P2_1/c$ and positional parameters in Table II, (c) calculated electron diffraction pattern.

ing the optical patterns, allowed to discard artifacts due to the microscope; in the same way, the images calculated by taking into account slight specimen tilt, or deviation of the center of the objective aperture or of the center of the optic axis did not generate the contrast actually observed. Moreover, when two orientation variants are present in the se-

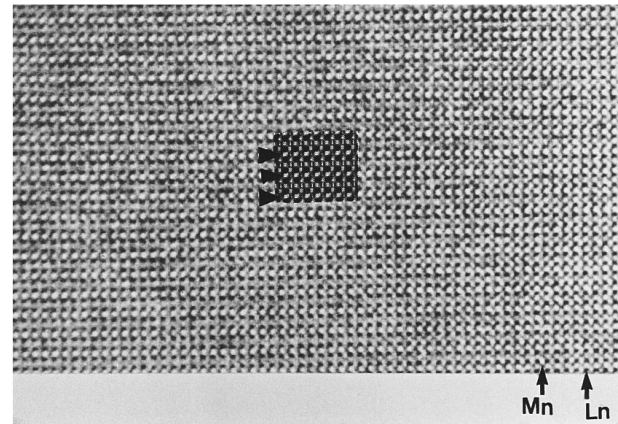


FIG. 5. HREM $[101]_o$ image where the heavy cation (Pr, Sr, and Ca) positions are imaged as darker dots (denoted L in the image) and the manganese positions as smaller grey dots; the 7.7 Å periodicity is clearly visible in the left part of the image, where one manganese row (indicated by black arrowheads) out of two exhibits a bright contrast whereas the other appears as a grey line. The simulated image, calculated for a monoclinic cell, is superposed to the experimental image.

lected objective aperture the doubling in HREM images is present in both variants.

The images recorded at different focus values suggest that the deviation from the perovskite structure particularly involves the $[\text{MnO}]_{2\infty}$ layer; this is deduced, e.g., from the thin sample in Fig. 5 where the dark dots are to be correlated to the positions of the heavy cations in twelfold coordination (they are denoted L in the image) whereas the small grey dots are correlated to the positions of the manganese atoms. In the left part of the image, where the doubling of the cell along b_o is observed, it clearly appears that the variation of contrast is observed in one $[\text{MnO}_2]_{\infty}$ layer out of two. This feature is also observed in all images. Note that such an unexpected contrast has been previously reported by Shibahara, *et al.*²² in LaMnO_{3-x} . However, these authors correlate the contrast variation to an oxygen deficiency in the $[\text{LaO}]_{\infty}$ layer, one oxygenated $[\text{LaO}]$ layer alternating with an oxygen free layer $[\text{La}]$ so that the formulation would be $\text{LaMnO}_{2.5}$; such a model which would involve Mn^{2+} seems unrealistic from a chemical point of view. At this stage, two alternative explanations can be considered: a variation of the contrast resulting from cation ordering in the complex $[(\text{Pr,Ca,Sr})\text{O}]_{\infty}$ layer, or a structural distortion.

The hypothesis of cation ordering as the origin of the effect has been investigated by comparing the $\text{Pr}_{0.7}\text{Ca}_{0.25}\text{Sr}_{0.05}\text{MnO}_3$ and $\text{Pr}_{0.75}\text{Sr}_{0.25}\text{MnO}_3$ images with those recorded for a similar “orthorhombic” manganese oxide exhibiting only a single type of cation, “ $\text{LaMnO}_{3.15}$ ” previously studied.^{23,24} The latter exhibits an identical contrast, with a clear doubling of the periodicity along b_o . Thus it can be concluded that even if Pr, Ca, and Sr are locally ordered, this ordering is not responsible for the particular contrast.

As to a possible structural distortion, the hypothesis of a noncentrosymmetric space group, $Pn2_1a$, has been investigated. In this group, the eight positions of the $\text{O}(2)$ site (Table I), which correspond to the oxygens located at the

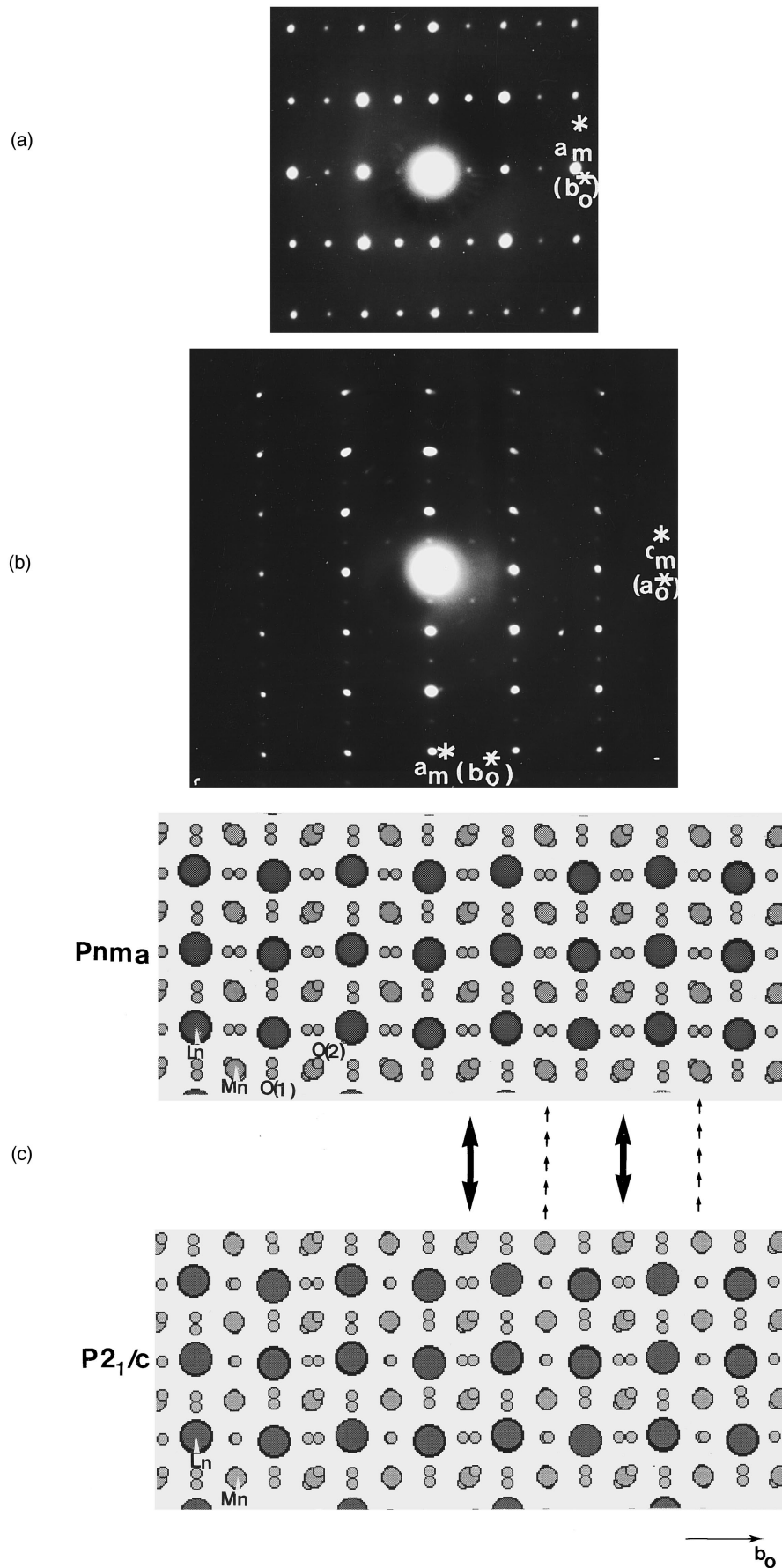


FIG. 6. (a) Evidence of a slight monoclinic distortion in (a) $[\bar{1}01]_o$ and (b) $[001]_o$ ED patterns. (c) $[101]_o$ projection of the orthorhombic structure for the atomic positions given in Table I compared to the equivalent projection of the monoclinic structure (SG $P2_1/c$) for the atomic positions given in Table II.

TABLE II. $\text{Pr}_{0.7}\text{Ca}_{0.25}\text{Sr}_{0.05}\text{MnO}_3$, $a_m=7.68 \text{ \AA}$, $b_m=5.44 \text{ \AA}$, $c_m=5.46 \text{ \AA}$, and $\beta=90^\circ+\varepsilon$, monoclinic cell, space group: $P2_1/c$, positional parameters.

Atom	x	y	z	Occup.
Pr	0.25	-0.006	0.033	0.7
Sr	0.25	-0.006	0.033	0.05
Ca	0.25	-0.006	0.033	0.25
Mn	0.500	0.50	0.00	1.0
Mn	0.000	0.00	0.50	1.0
O(1)	0.25	0.07	0.486	1.0
O(2)	0.483 ^a	-0.285	0.287	1.0
O('2)	0.037	-0.285	0.287	1.0

^a x value which has been varied.

level of the manganese, are split into two groups of four positions, so that the z values of these oxygens can be dissociated. The image calculations evidence that a contrast variation is thus generated but it still strongly differs from the experimental one presented in Figs. 3(a) (area 2), 3(b) and 5. To deduce the presence, or not, of an inversion center, convergent beam ED has been used but no clear answer could be provided by this technique, probably due to the presence of point defects (see further).

Careful inspection of the selective area ED patterns from areas where the doubling effect is strong, evidence a slight distortion in the angle between the $[101]_o^*$ and $[010]_o^*$ vectors; in Fig. 6(a) the β angle is close to 90° . From the ED study carried out on several crystals and crystal zones, the actual cell symmetry of the structure corresponding to these

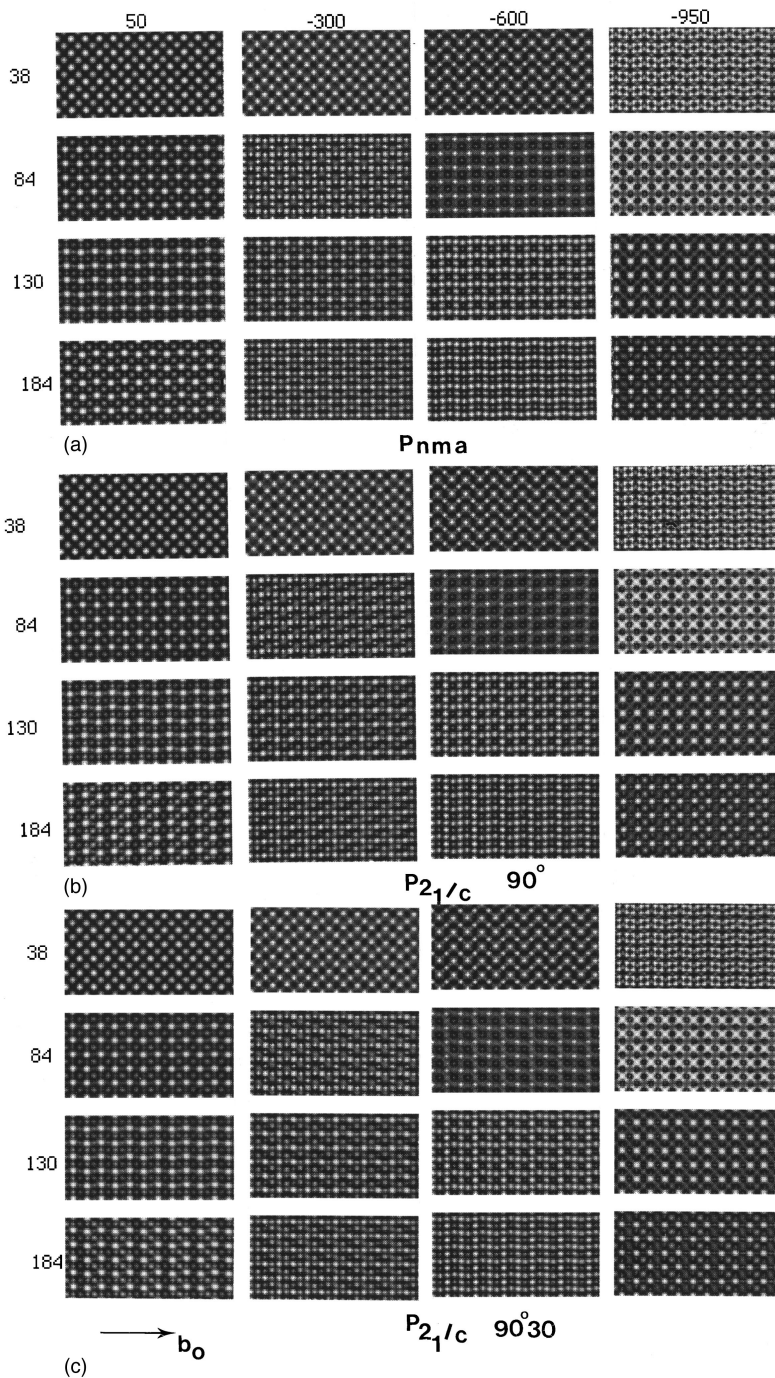


FIG. 7. Calculated images vs crystal thickness (in \AA): (a) orthorhombic cell, SG: $Pnma$ (b) monoclinic cell: $P2_1/c$ with $x_{\text{O}(2)}=0.49$ instead of 0.463 and $\beta=90^\circ$, (c) monoclinic cell: $P2_1/c$ with $x_{\text{O}(2)}=0.49$ and $\beta=90^\circ$ 3.

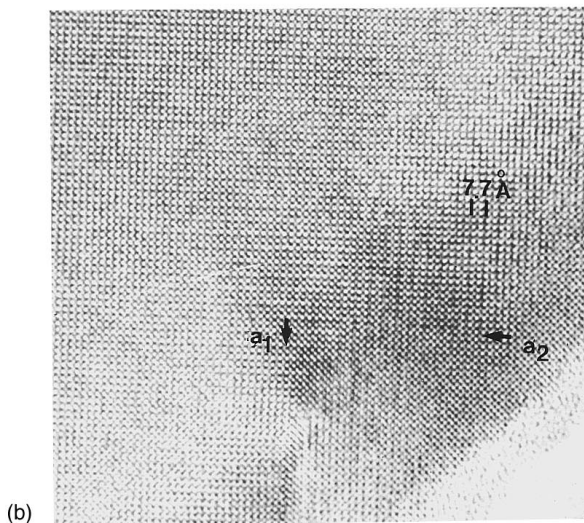
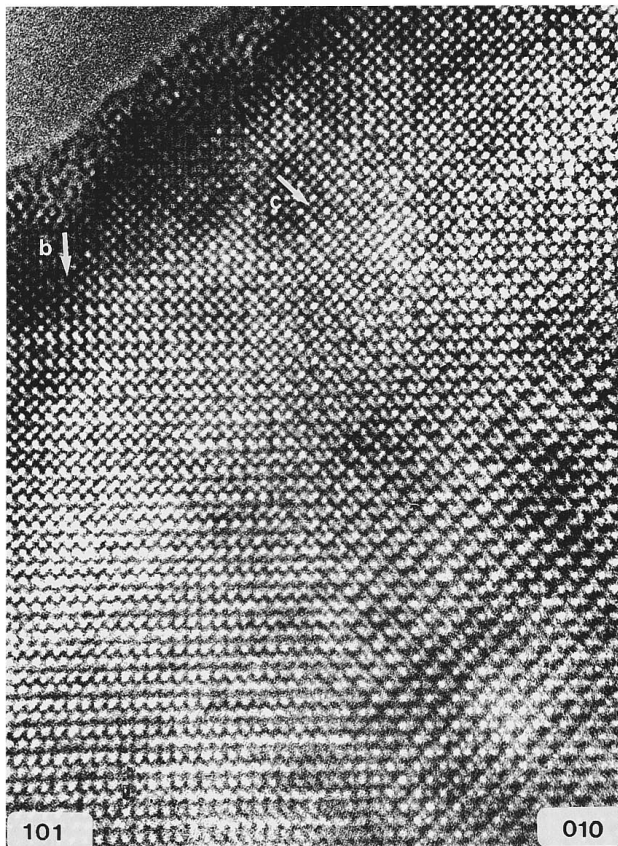


FIG. 8. (a) $[101]_o$ and $[010]_o$ large oriented domains (axes referring to the orthorhombic cell) and (b) $90^\circ [011]_m$ oriented domains labeled 1 and 2 (axes referring to the monoclinic cell).

images would be monoclinic, the cell parameters being $a_m \approx b_o \approx 7.68 \text{ \AA}$, $b_m \approx c_o \approx 5.44 \text{ \AA}$, $c_m \approx a_o \approx 5.46 \text{ \AA}$, and β varying between $90^\circ 0$ and $90^\circ 3$. The $[010]_m$ ED pattern of this monoclinic cell is given in Fig. 6(b); it corresponds to the $[001]_o$ pattern of the orthorhombic structure. The relationship between the orthorhombic and the monoclinic cells are shown in Fig. 6(c). Image simulations have been carried out to check the contrast variation induced by such a breakdown of the symmetry. Considering the $P2_1/c$ space group, every cation is in a $4e$ site $(x, y, z; \bar{x}, \bar{y}, \bar{z}; \bar{x}, 1/2 + y, 1/2 - z; x, 1/2 - y, 1/2 + z)$; two different sites $O(2)_m$ and $O(2)'_m$ generate the eight positions of the $O(2)_o$ site of the orthorhombic $Pnma$ structure. The positional parameters of Pr, O(1), and O(2) are absolutely identical in both the orthorhombic and the monoclinic cell whereas the $O'(2)_m$ sites correspond to different atomic positions with respect to the O(2) sites but become rigorously identical to the latter for particular $x_{O'}$ values corresponding to the relation $x = \frac{1}{2} - x_{O(2)}$.

Starting from the ideal atomic positions deduced from the orthorhombic cell, with $x_{O(2)} = 0.463$, the influence of the variation of the $x_{O(2)}$ value upon the contrast of the HREM image has been investigated. For $x_{O(2)} = 0.463$ and $\beta = 90^\circ$, the calculated images are similar to those presented in Fig. 4(a), in agreement with the orthorhombic symmetry of the structure generated by these particular parameters. Next only the $x_{O(2)}$ position was varied from 0.47 (y value in the orthorhombic structure) to 0.50, leaving the other atomic positions and keeping $\beta = 90^\circ$. Finally, we varied the position of the $O(2)_m$ site from 0.47 to 0.53, simultaneously with the β angle from 90° to $90^\circ 3$. As soon as the x value of the two $O(2)_m$ sites is varied, i.e., when $x'_{O(2)}$ is no longer equal to $1/2 - x_{O(2)}$, a variation of the contrast, and especially the effect of doubling, is observed.

An example of through focus series, calculated in the $P2_1/c$ group, is shown in Fig. 4(b) for the atomic positions listed in Table II. These positions differ from the orthorhombic structure only by the $x_{O(2)}$ value of 0.49 (instead of 0.463), the β angle being kept to 90° . The crystal thickness is 12 nm in order to make easy a direct comparison with the images calculated for the $Pnma$ structure [Fig. 4(a)]. These simulated images are characterized by a contrast variation (with regard to the $Pnma$ images) which is in perfect agreement with the experimental contrast (Figs. 3 and 5). The calculated ($\Delta f \approx -200 \text{ \AA}$) and experimental images are superimposed in Fig. 3(b) where the low electron density zones appear as bright dots. The 7.7 \AA periodicity arises from the replacement of one row of bright dots by a row of grey dots [indicated by a small black arrowhead in Fig. 4(b)] which are correlated to the $O(2)_m$ position. One observes that the contrast is slightly amplified as the monoclinic distortion increases. Selecting four focus values, the contrast variation vs crystal thickness is shown in Fig. 7 for the orthorhombic ($Pnma$) cell and the monoclinic ($P2_1/c$) cell with $\beta = 90^\circ$ and $90^\circ 3$. Another example confirming that the effect results from a variation of the manganese environment in one $[\text{MnO}_2]_\infty$ layers out of two is given in Fig. 5 where the superposition of the calculated image shows that the contrast fits well with the experimental one.

More detailed interpretation of the images would need accurate oxygen positions. The hypothesis of a monoclinic symmetry has been introduced in the neutron-diffraction data;²⁰ one observes an anisotropy of the reflection widths which is in agreement with the existence of a monoclinic symmetry of at least a part of the sample. From this HREM study, accurate oxygen positions cannot indeed be determined but the important fact is the breakdown of the orthorhombic symmetry.

The projection of the orthorhombic structure along $[101]_o$ [Fig. 6(a)] compared to the equivalent projection of

the monoclinic structure [Fig. 6(b)] clearly shows that one manganese oxygen layer out of two is identical in both structures (indicated by large arrows) whereas the second manganese oxygen layer is modified (indicated by small arrows).

Other image calculations have been carried out varying the other coordinates y and z of the atoms located in the O(2) site and varying also the x value of the O(1) site, but none of these attempts led to a so significant variation of the contrast, compared to that generated by varying the $x_{O(2)}$ value.

The projections of the two structures along \mathbf{b}_o are similar so that the orthorhombic and monoclinic structures cannot be differentiated along this direction, this is in agreement with the simulated images. The experimental $[010]_o$ images are similar to those usually observed in classical perovskites. In contrast, the $[100]_o$ direction should be suitable to distinguish both structures, since the reflection conditions are different: $0kl, k+l=2n$ for the orthorhombic and $0k0, k=2n$ for the monoclinic structures, respectively. Unfortunately, the existence of oriented domains involving the superposition of different systems, and the too small deviation from the orthorhombicity for the monoclinic structure do not allow the two structures to be differentiated; this is shown by the experimental images and confirmed by the simulated $[010]_o$ images.

Local distortions, domains and boundaries

As mentioned in the above section, few ED patterns can be recorded avoiding the superposition of at least two different systems. The fact that the superstructure reflections which arise from the orthorhombic GdFeO_3 -type distortion can be observed along the equivalent directions of the perovskite subcell is a feature which has been observed in numerous similar systems. But, in the case of $\text{Pr}_{0.7}\text{Ca}_{0.25}\text{Sr}_{0.05}\text{MnO}_3$ and $\text{Pr}_{0.75}\text{Sr}_{0.25}\text{MnO}_3$, the observations reported in the above section show that along particular directions, monoclinic distortions, and superposed domains lead to similar ED patterns and images; this observation is confirmed by ED pattern and image calculations.

The domain sizes range from a few nanometers to some thousand and the nature of the boundary depends on the orientation; two examples are given in Fig. 8. The first one corresponds to large $[010]_o$ and $[101]_o$ oriented domain [Fig. 8(a)]; the boundary is clear but not straight and wanders in the thicker part. In Fig. 8(b), the very small $[011]_m$ domains result from two 90° orientations of the monoclinic superstructure. The boundaries are in fact so broad that sometimes the contrast is modified and corresponds to a simple perovskite structure; this feature is similar to that observed in Fig. 3(a) between $[011]_m$ and $[101]_o$ domains.

Another type of boundary can be observed within the $[011]_m$ domains [Fig. 9(a)]. Two areas, labeled 1 and 2, exhibit parallel \mathbf{a}_m axes but the two matrices are shifted by a_p , i.e., by $a_m/2$ through an antiphase boundary (APB); this is clearly observed by viewing the image at grazing incidence and referring to the two black lines schematically drawn in Fig. 9(b). In the right part of Fig. 9(a), this translation is no more observed. At the junction between the two domains a defective structure is observed where three adjacent rows of bright dots (white arrowhead), instead of two are locally formed. This defect can be interpreted as a twin

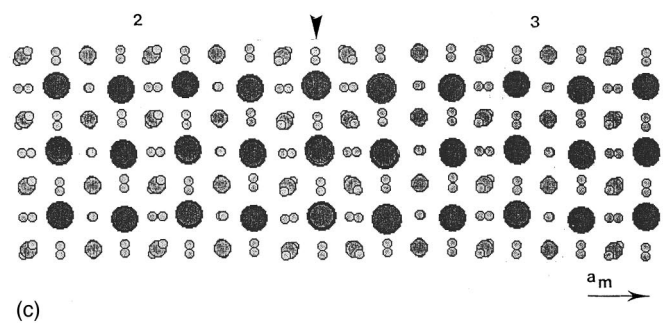
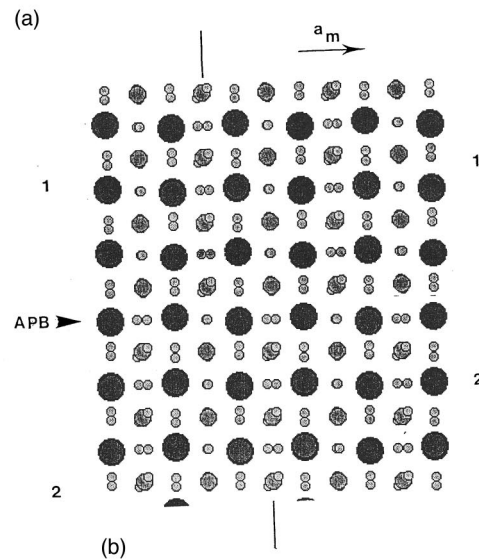
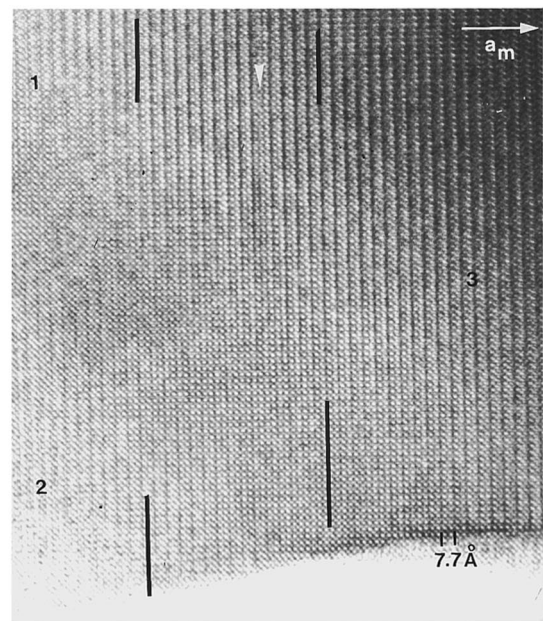


FIG. 9. (a) $[011]_m$ image of a monoclinic crystal where an antiphase boundary (APB) is observed; the ordering of zone 1 is translated by $a_m/2$ with regard to zone 2. In area 3, this translation is no more observed; the junction is ensured through a defective layer (indicated by a white arrowhead). (b) model of the APB between areas 1 and 2. (c) model of the defective layer between areas 2 and 3.

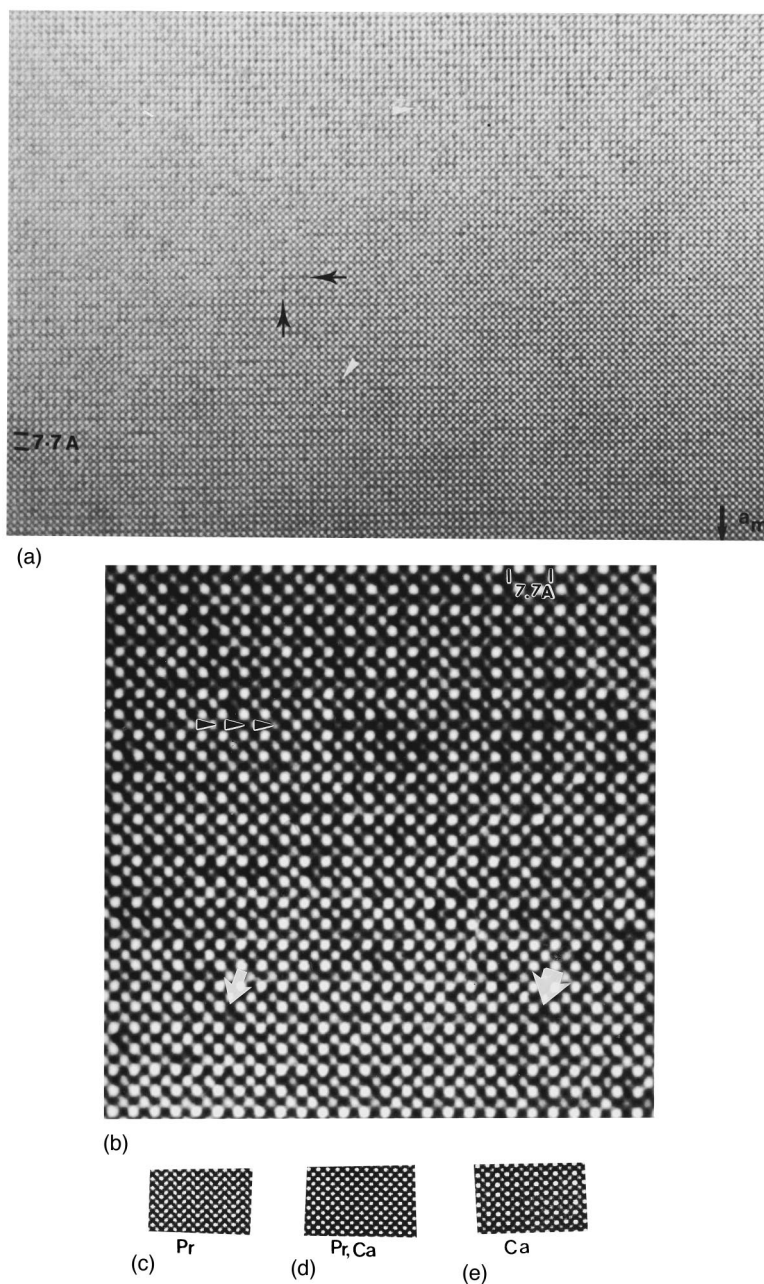


FIG. 10. Typical $[101]_o$ (a) overall and (b) enlarged images of pointlike defects: the intensity of the bright dots correlated to the manganese positions varies. These variations are preferentially observed at the level of the Mn atoms surrounded by O(2) but some variations are also observed at the level of those surrounded by O'(2); two of them are indicated by white arrowheads. These defects are often regrouped in short linear segments running along $[100]_m$ as well as along $[011]_m$; they are indicated by black arrows. Comparison between the calculated images for (c) PrMnO_3 , (d) $\text{Pr}_{0.7}\text{Ca}_{0.25}\text{Sr}_{0.05}\text{MnO}_3$, and (e) CaMnO_3 .

boundary, it is schematically represented in Fig. 9(c); the boundary (black arrowhead) corresponds to a $[LO]$ layer; it plays the role of mirror so that it involves the local formation of two adjacent manganese layers which exhibit the orthorhombic-type distortion.

Clustering phenomena

A very important feature that characterizes both samples, $\text{Pr}_{0.7}\text{Ca}_{0.25}\text{Sr}_{0.05}\text{MnO}_3$ and $\text{Pr}_{0.75}\text{Sr}_{0.25}\text{MnO}_3$, deals with the existence of isolated pointlike defects, that systematically appear. Such "point defects" are clearly visible in the overall and enlarged $[101]_o$ images displayed in Figs. 10(a) and

10(b), respectively, where the bright dots are correlated to the positions of the Pr and Ca or Sr sites and the smaller ones to the manganese atoms. Whereas the intensity of the (Ln,A) sites is very constant, the intensity of the Mn dots varies considerably within a limited area [see, e.g., the darker dots indicated by white arrows in Figs. 10(a) and 10(b)].

This type of defect is observed in the thin part of the crystal as well as in the thicker parts [Fig. 10(a)] where the contrast evidences a monoclinic structure; if we consider the two types (cf. Table II) of manganese layers in the monoclinic structure, i.e., those surrounded by O(2) (distorted octahedra similar to those in the GdFeO_3 -type structure) and those by O'(2) (less distorted octahedra), the modification

of contrast is preferentially observed in the first type but some variations are also observed in the second one; two of them are indicated by white arrows in Figs. 10(a) and 10(b). The density of defects does not increase during the observation and their contrast is not modified so that we can exclude the idea that they are generated by electron-beam irradiation.

Three kinds of defects may produce such a contrast variation: (i) vacancies or atomic substitution on the manganese sites, (ii) oxygen vacancies in the MnO_6 octahedra, (iii) variation of the oxygen environment around the manganese.

The neutron-diffraction studies of these phases,²⁰ and the EDS analysis show that these compounds do not exhibit a significant deviation from stoichiometry for oxygen as well as for manganese, so that the rather large density of defects observed in these materials can only be explained by a local modification of the manganese environment. Taking into consideration the mixed valence Mn(III)-Mn(IV) of manganese, such a variation of the contrast may be closely related to a local ordering of the Mn(III) and Mn(IV) species, so that a variation of the Mn-O distances around the manganese would be involved, in agreement with the different sizes of the Mn(III) and Mn(IV). Moreover the geometry of the Mn(III) octahedra will be different from that of the Mn(IV) octahedra, owing to its Jahn-Teller effect. It is, of course, not possible to propose new positional parameters of these sites because of the interaction with the surrounding matrix. Nevertheless, images can be simulated for the limit structures PrMnO_3 (Ref. 25) [Fig. 10(c)] and CaMnO_3 (Ref. 26) [Fig. 10(e)] that correspond to pure Mn(III) and Mn(IV) perovskites, respectively. Such images, calculated for the 50 Å focus value, which correspond to that of the experimental image of Fig. 10(b), can be compared to the simulated image of $\text{Pr}_{0.7}\text{Ca}_{0.25}\text{Sr}_{0.05}\text{MnO}_3$ [Fig. 10(d)], calculated for the same focus value.

For this focus value, the bright dots are correlated to the Pr and Ca positions, and the manganese atoms in CaMnO_3 are imaged as very small grey dots, scarcely visible, whereas in PrMnO_3 and orthorhombic $\text{Pr}_{0.7}\text{Ca}_{0.25}\text{Sr}_{0.05}\text{MnO}_3$ they

are imaged as rather bright dots. Thus, the appearance of darker spots around manganese sites [Figs. 10(a) and 10(b)] in the matrix may be explained by a modification of the geometry of the MnO_6 octahedra due to an electronic localization forming Mn(IV) species.

Another important feature deals with the fact that these darker dots are often regrouped in short linear segments, a few octahedra long, along $[100]_m$, i.e., $[010]_o$ as well as along $[011]_m$, i.e., $[101]_o$; this could be a way to decrease the strains introduced by these defects. The isolated and linear defects, can therefore be described as $(A^{II}\text{Mn}^{IV}\text{O}_3)_n$ clusters distributed in the mixed-valent Mn(III)-Mn(IV) perovskite matrix in a random way. No further signs of ordering of these clusters has been detected by electron diffraction. Contrary to what has been reported in $\text{La}_{0.8}\text{Sr}_{0.2}\text{MnO}_3$,²⁷ no linear defect involving Ln/A vacancy defects has been detected.

CONCLUDING REMARKS

This study of the praseodymium perovskites shows two structural features which may be of capital importance to understand the CMR properties of these materials. The first one deals with the existence of monoclinic microdomains in the orthorhombic GdFeO_3 -type matrix; the latter demonstrates the high flexibility of the structure or more exactly of the $[\text{MnO}_2]_\infty$ layers, so that the coordination of manganese may be easily changed according to its local electronic configuration. Such a high flexibility may favor the magnetic transitions observed in these oxides.²⁰ The second feature deals with the existence of $(A^{II}\text{Mn}^{IV}\text{O}_3)_n$ clusters corresponding to a modification of the geometry of the MnO_6 octahedra with respect to the matrix. Such clusters where size and distribution may vary with the temperature, may be connected with the variation of the Jahn-Teller effect of manganese that has been observed at the ferromagnetic transition.²⁰ An electron microscopy study of these materials below the transition temperature will be necessary to understand the role of these structural anomalies in the CMR properties of these oxides.

*EMAT, University of Antwerp (RUCA), Groenenborgerlaan, 171, B-2020 Antwerpen, Belgium.

¹R. M. Kusters, J. Singleton, D. A. Keon, R. M. Greedy, and W. Hayes, *Physica B* **155**, 362 (1989).

²K. Chahara, T. Ohno, M. Kasai, and Y. Kozono, *Appl. Phys. Lett.* **63**, 1990 (1993).

³R. Von Helmolt, J. Wecker, B. Holzapfel, L. Schultz, and K. Samwer, *Phys. Rev. Lett.* **71**, 2331 (1993).

⁴S. Jin, T. H. Tiefel, M. McCormack, R. A. Fastnacht, R. Ramesh, and L. H. Chen, *Science* **264**, 413 (1994).

⁵M. McCormack, S. Jin, T. H. Tiefel, R. M. Fleming, J. M. Phillips, and R. Ramesh, *Appl. Phys. Lett.* **64**, 3045 (1994).

⁶H. L. Ju, C. Kwon, Q. Li, R. L. Greene, and T. Venkatesan, *Appl. Phys. Lett.* **65**, 2108 (1994).

⁷S. S. Manoharan, N. Y. Vasanthacharya, M. S. Hedge, K. M. Satyalakshmi, V. Prasad, and S. V. Subramanyam, *J. Appl. Phys.* **76**, 3923 (1994).

⁸G. C. Xiong, Q. Li, H. L. Ju, R. L. Greene, and T. Venkatesan, *Appl. Phys. Lett.* **66**, 1689 (1995).

⁹G. C. Xiong, Q. Li, H. L. Ju, S. N. Mao, L. Seanapati, X. X. Xi, R. L. Greene, and T. Venkatesan, *Appl. Phys. Lett.* **66**, 1427 (1995).

¹⁰R. Mahesh, R. Mahendiran, A. K. Raychandhuri, and C. N. R. Rao, *J. Solid State Chem.* **114**, 297 (1995).

¹¹S. Jin, H. M. O'Bryan, T. H. Tiefel, M. McCormack, and W. W. Rhodes, *Appl. Phys. Lett.* **66**, 382 (1995).

¹²A. Maignan, V. Caignaert, Ch. Simon, M. Hervieu, and B. Raveau, *J. Mater. Chem.* **5**, 1089 (1995).

¹³V. Caignaert, A. Maignan, and B. Raveau, *Solid State Commun.* **95**, 357 (1995).

¹⁴B. Raveau, A. Maignan, and V. Caignaert, *J. Solid State Chem.* **117**, 424 (1995).

¹⁵A. Maignan, Ch. Simon, V. Caignaert, and B. Raveau, *C. R. Acad. Sci.* **321**, 297 (1995).

¹⁶H. Y. Hwang, S. W. Cheong, P. G. Radaelli, M. Marezio, and B. Battlog, *Phys. Rev. Lett.* **75**, 914 (1995).

¹⁷A. Maignan, Ch. Simon, V. Caignaert, and B. Raveau, *Z. Phys. B* **99**, 305 (1996).

- ¹⁸A. Maignan, Ch. Simon, V. Caignaert, and B. Raveau, *Solid State Commun.* **96**, 623 (1995).
- ¹⁹G. Q. Gong, C. Canedy, G. Xia, J. Z. Sun, A. Gupta, and W. J. Gallagher, *Appl. Phys. Lett.* **67**, 1783 (1995).
- ²⁰V. Caignaert, E. Suard, A. Maignan, Ch. Simon, and B. Raveau, *J. Magn. Magn. Mater.* (to be published).
- ²¹S. Geller and A. E. Wood, *Acta Crystallogr.* **9**, 563 (1956).
- ²²H. Shibahara, K. Numaguchi, M. Kawasaki, M. Takizawa, and T. Oikawa, *Electron Microscopy* **13**, 871 (1994)..
- ²³H. Hervieu, R. Mahesh, N. Rangavittal, and CNR Rao, *Eur. J. Solid State Inorg. Chem.* **32**, 79 (1995).
- ²⁴J. A. M. Van Roosmalen, E. H. P. Cordfunke, and R. B. Helmholtz, *J. Solid State Chem.* **110**, 100 (1994).
- ²⁵V. A. Cherepanov, L. Yu. Barkhatova, A. N. Petrov, and V. I. Voronin, *J. Solid State Chem.* **118**, 53 (1995).
- ²⁶K. R. Poeppelmeier, M. E. Leonowicz, J. C. Scanlon, J. M. Longo, and W. B. Yelon, *J. Solid State Chem.* **45**, 71 (1982).
- ²⁷H. Cerva, *J. Solid State Chem.* **114**, 211 (1995).